Electronic Supplementary Material (ESI) for Journal of Materials Chemistry C.

Supporting Information

A highly transparent ion conducting film enabling visual electrochromic battery

Wanzhong Li, Ting Bai, Qianqian Zhang, Jingbing Liu, Kailing Zhou, Hao Wang**

Content of Supporting Information

1. The porosity of PVDF matrix and ionic conductivity (σ) of ICF

The porosity of PVDF film was measured by using N-butanol-immersion method, which could be determined based on the equation S1 [1]:

$$\text{Porosity (\%)} = (W-W_0)/(\rho\times V_0) \qquad \text{(S1)}$$

In this equation, W and W_0 were the weights of N-butanol-immersion PVDF and dry PVDF, respectively. ρ meant the density of N-butanol and V_0 was the volume of PVDF.

The ICF was sandwiched between two stainless steels barrier electrodes. And the σ was calculated using the equation S2 [1]:

$$\sigma = LA/R \qquad \text{(S2)}$$

where R is the bulk resistance (Fig. 1g), L and A are the thickness and area of the ICF, respectively.

2. Nitrogen adsorption–desorption isotherms of PVDF membranes.

As presented in Figure S1a, the PVDF membranes exhibited a reversible type III isotherm with no hysteresis, which was determined to be a typical mesoporous material. The BET surface area of PVDF membranes were 8.86 m^2 g^{-1} with a uniform pore size distribution (≈4.5 nm) and pore volume (≈0.03 cm^3 g^{-1}) (Figure S1b).

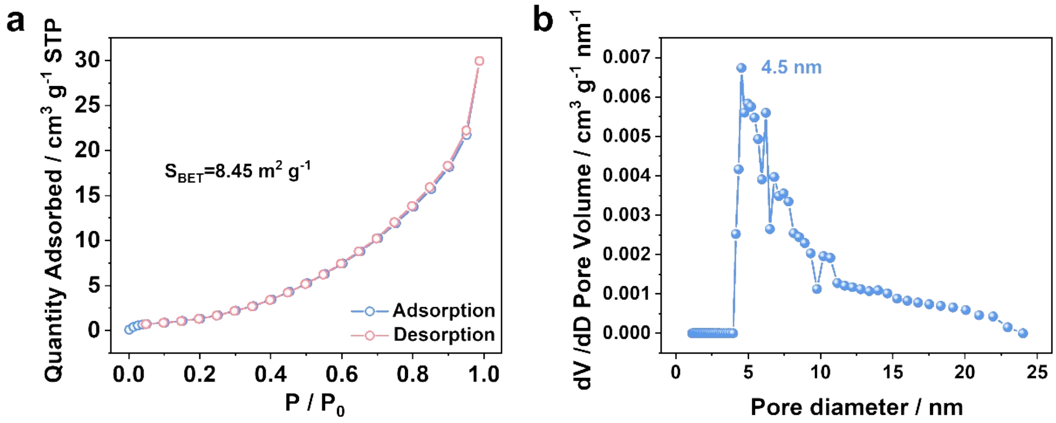

Figure S1. (a) Nitrogen adsorption–desorption isotherms of PVDF membranes. (b) Pore sizes distribution of PVDF membranes.

3. Transmittance spectra of ICF with different thickness (30 µm, 55 µm, 70 µm and 80 µm), named as sample 1 to 4

The PVDF-based ICF with different thickness presented high transmittance over 90% in region from 350 nm to 1100 nm. Especially, the transmittances of both samples are above 90% at a wavelength of 550 nm and 850 nm, respectively.

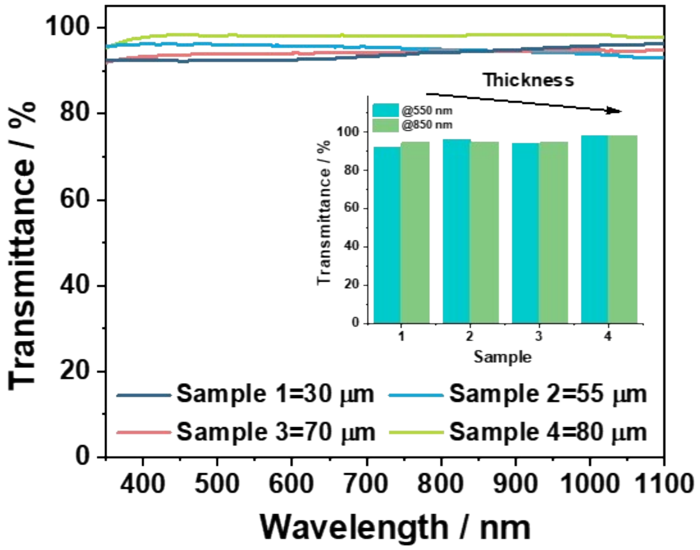

Figure S2. Comparative transmittance spectra of ICF with different thickness (30 µm, 55 µm, 70 µm and 80 µm), named as sample 1 to 4. Inset shows calculated transmittance values for samples with different thickness at a wavelength of 550 nm.

4. The mechanical properties of the PVDF matrix

Tensile stress-strain curve of the PVDF matrix with different thickness (30 μm, 55 μm, 70 μm and 80 μm) was recorded in Figure S3a, to examine the mechanical properties of ICF. The tensile strength of a 30-μm-thick PVDF matrix is 3.9 MPa, with a Young's modulus of 2.1 MPa (Figure S3a, b). By increasing the thickness of the polymer matrix to 80 μm, tensile strength is improved to 6.8 MPa, while the Young's modulus reaches to 9.5 MPa. Obviously, the PVDF polymer matrix with thickness of 80 μm exhibit the optimal mechanical strength. The excellent mechanical strength is advantageous for the construction of the large area EC device.

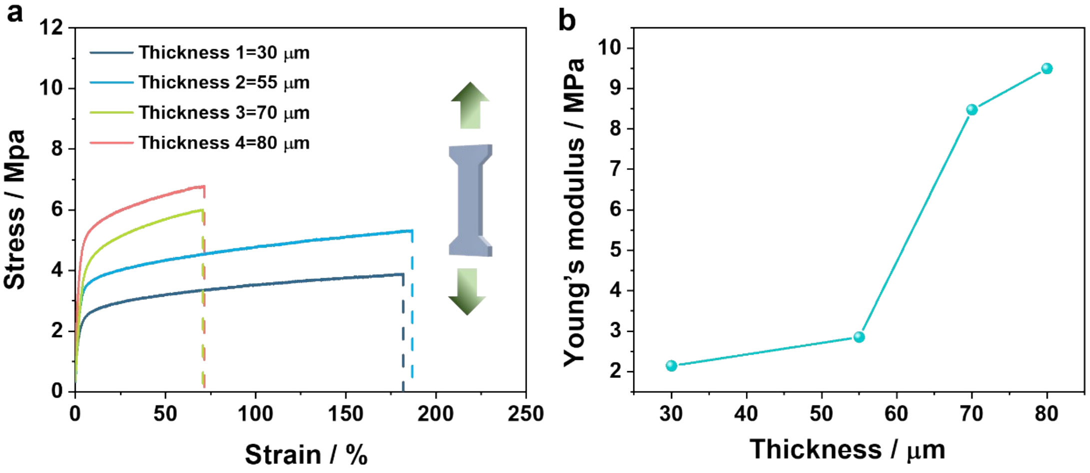

Figure S3. (a) Tensile stress-strain curve of the PVDF matrix with different thickness. The inset exhibits the schematic diagram of stretching process. (b) Calculated Young's modulus of the PVDF matrix with different thickness.

5. A comprehensive comparison of the transmittance and lithium ion conductivity of the ICF with other currently used electrolytes or films

Figure S4 provided the comprehensive comparison of the optical transmittance and lithium ion conductivity of the currently used electrolytes and the ICF in this work. Clearly, the ICF could offer a transparency over 90% and relatively high ionic conductivity of 0.46 mS cm^{-1}, comparable with some recent state-of the-art works [2-8].

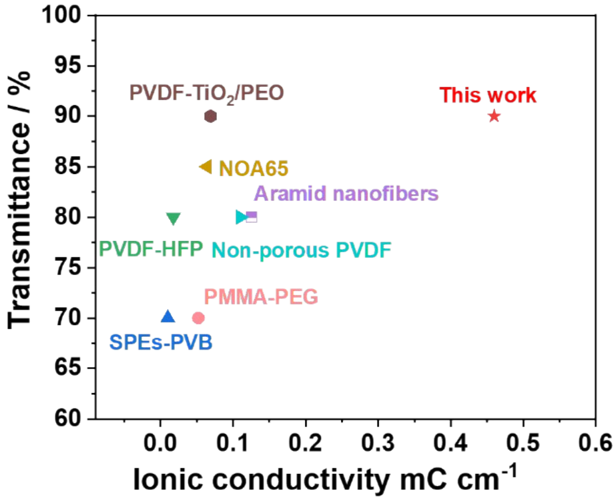

Figure S4. Comparisons on the ionic conductivity and transmittance for the ICF developed in this work and other reported electrolyte or films.

6. Surface and EDS elemental distribution of LMO film

As shown in Figure S5, the LMO film was assembled by uniform granules with the width of 500 nm, possessing some 3D porous channels among these granules. This structure could provide direct transport channels for the fast Li^+ insertion or extraction.

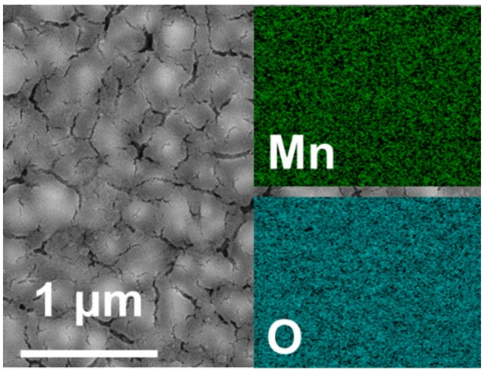

Figure S5. Surface and EDS elemental distribution in selected areas of LMO EC film.

7. Transmittance spectra of charging/discharging LMO electrode

LMO electrode had a good optical modulation in the wavelength region from 400-1100 nm, and presented a red shift from initial yellowish-brown to orange-red after charged (digital photo in the inset of Figure S6).

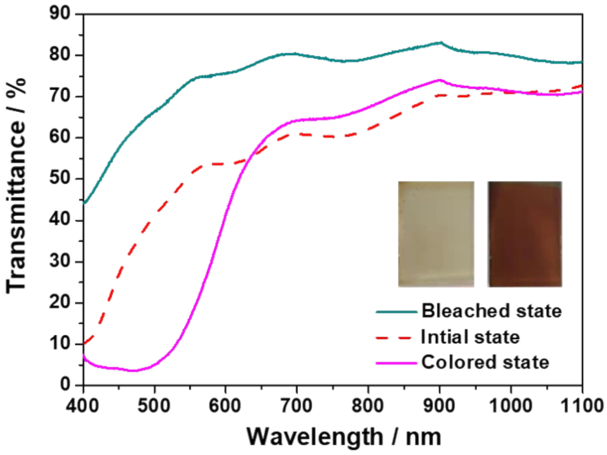

Figure S6. Transmittance spectra of LMO electrode in the charged and discharged states in the wavelength from 400 to 1100 nm (Insets: Optical photographs of the electrode switching between two states

8. The coloring/bleaching switching time and coloring efficiency (CE) of LMO and LTO electrode

Figure S7a shows the change of transmittance at 550 nm in several cycles, the bleaching time and coloring time of LMO film are 41 s and 42 s, respectively. And the LTO film is 52 s (coloring time) and 42 s (bleaching time), respectively. The close switching time demonstrated the consistency in the kinetic behavior of the electrochemical reaction of LMO and LTO films. In addition, CEs of LTO electrode, LMO electrode are presented in Figure S7b and d. The calculated CE of the LMO electrode was about 32.91 cm2C^{-1} at 550 nm (Figure S7b). The calculated CEs of the LTO electrode were about 8.23 cm^{2}C^{-1} at 550 nm and 30.05 cm^{2}C^{-1} at 850 nm (Figure S7d), respectively.

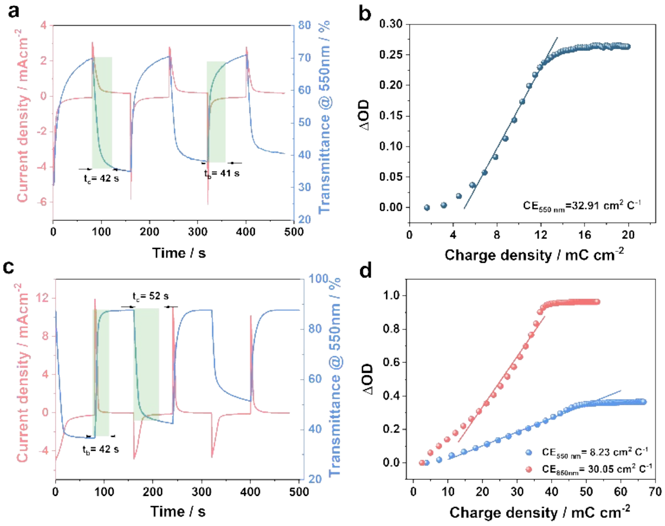

Figure S7. EC performance of LMO film: (a) Chronoamperometry curve and the corresponding in situ transmittance curve at 550 nm. (b) Optical density (ΔOD) as a function of charge density. EC performance of LTO film: (c) Chronoamperometry curve and the corresponding in situ transmittance curve at 550 nm. (d)ΔOD as a function of charge density.

9. The energy storage performance of the LMO electrode.

Moreover, the charging and discharging profiles of the LMO at the same potential window ranging from 0.1 to 0.8 mA cm^{-2} are presented in Figure S8a. LMO demonstrated flat and long operating voltage plateaus. The corresponding areal capacity of LTO and LMO was calculated from Figure S8b. Both areal capacities showed a decreasing trend as the current density increased due to insufficient reaction at the large current density [9]. Meanwhile, the LTO and LMO films had the almost equal capacity ranging from 0.1 to 0.8 mA cm^{-2}.

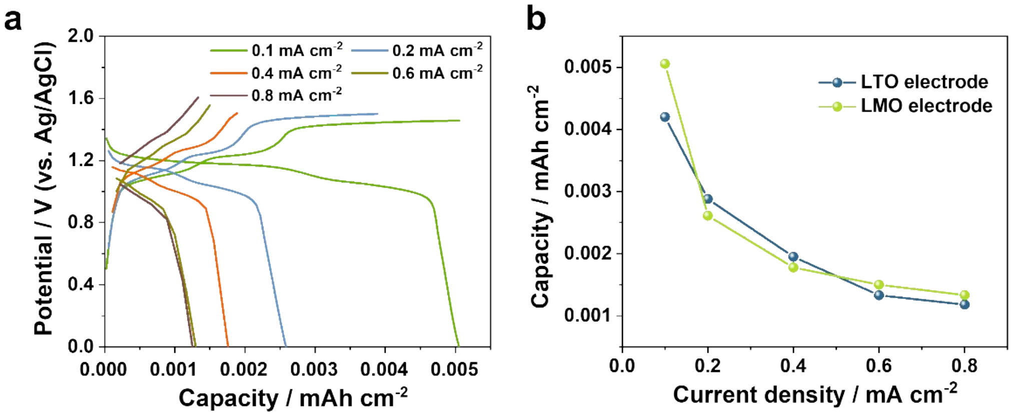

Figure S8. (a) Charging and discharging profiles of LMO electrode at various current densities. (b) Corresponding areal capacity matching of LTO and LMO films.

10. CV curves of LMO electrode at different scan rates and corresponding in-situ transmittance spectra

The *in-situ* transmittance and corresponding CV curves at 5 mV s^{-1} were recorded in Figure S9a. Notably, the LMO film decreased from 72.9% to 26.5% at the wavelength of 550 nm when the potential reached to 1.5 V. Moreover, the transmittance still could recover to around the initial value after reverse scan process, suggesting the highly reversible charging/discharging process of LMO. Figure S9b showed the typical CV curves of LMO electrode within a potential window of -0.5 V ~ 1.5 V (vs. Ag/AgCl) at different scan rates. The CV behaviors of the LMO anode showed three pairs of typical redox peaks below 1.5 V, which were corresponding to the reversible Li-ions insertion/extraction within the spinel structure into different stages [10].

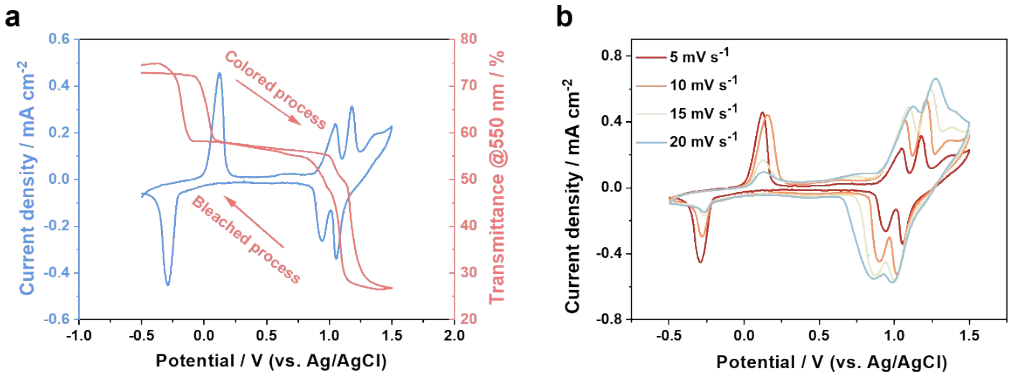

Figure S9. (a) *In-situ* transmittance and corresponding CV curves at 5 mV s^{-1}. (b) CV curves of LMO electrode at different scan rates.

11. CV profiles of ICF-ECB measured at different working voltages

Figure S10 depicted series of CV profiles with different working windows were measured at 10 mV s^{-1}, which revealed the ICF-ECB could effectively operate in a stable electrochemical behavior at 3.2 V.

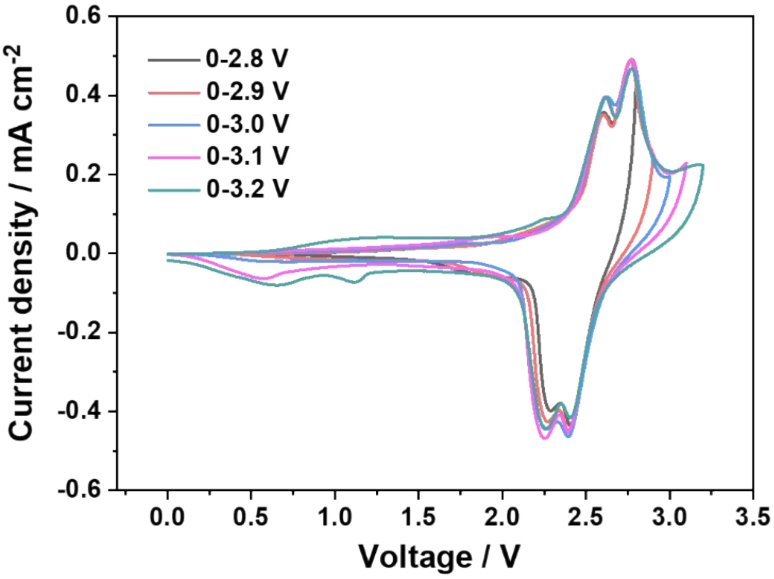

Figure S10. CV profiles of ICF-ECB measured at different working voltages from 2.8 V to 3.2 V at 10 mV s^{-1}.

12. Power density and energy density of ICF-ECB in this work compared with several reported energy storage devices.

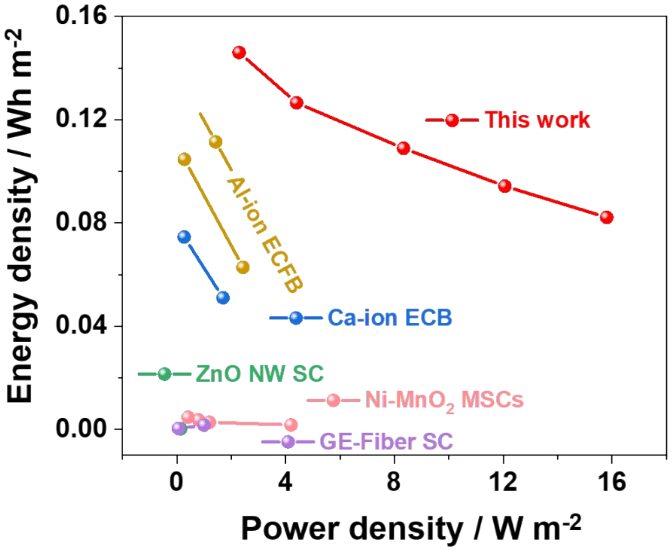

Figure S11. Ragone plots of ICF-ECB in this work compared with several reported energy storage devices[11-15].

13. Open-circuited memory effect of the charged ICF-ECB after open circuit

As shown in Figure S12, the ICF-ECB could keep coloring state for 8 h and achieve the $\Delta T_{retention}$ =36.9%, exhibiting an outstanding open-circuit memory effect.

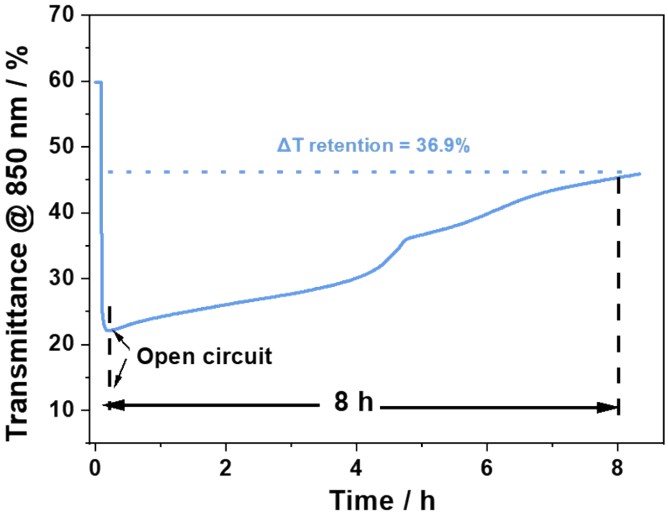

Figure S12. Open-circuited memory effect of the charged ICF-ECB after open circuit.

14. Cycling stability in the transmittance variations and current density in response to periodical charging and discharging

Figure S13 recorded the transmittance variations at 850 nm and current density of ICF-ECB after 200 charging/discharging cycles between 0 V and 3 V, which demonstrated the excellent cycle stability of the obtained device.

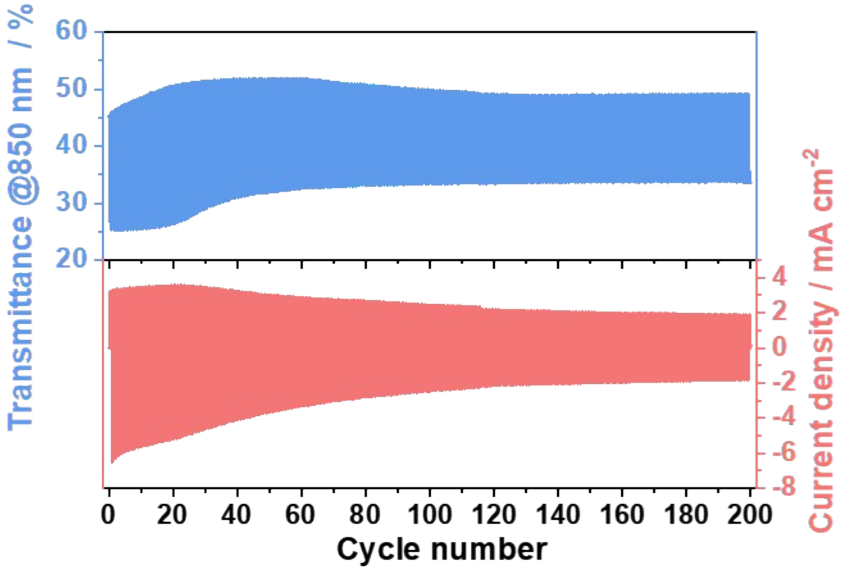

Figure S13. Cycling stability of the ICF-ECB with respect to periodic charging/discharging.

15. A long-term GCD cycling measurement of ICF-ECB

In order to evaluate the long-term cyclic test regarding charging/discharging ability of the ICF-ECB, a long-term GCD cycling measurement was carried out at 0.2 mA cm^{-2} (Figure S14).

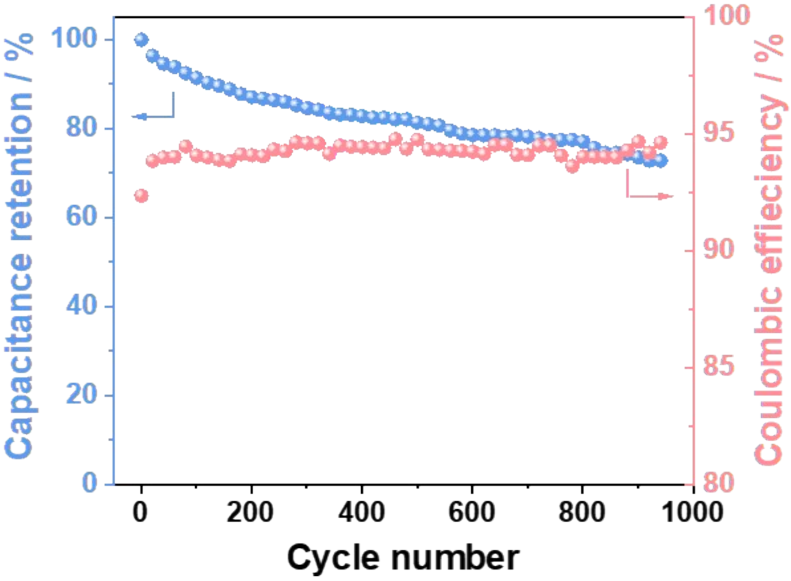

Figure S14 Cycling performance of the ICF-ECB at 0.2 mAcm^{-2} for 1000 cycles.

16. References:

[1] Q. Zhao, R. Zhou, C. Wang, J. Kang, Q. Zhang, J. Liu, Y. Jin, H. Wang, Z. Zheng and L. Guo, *Adv. Funct. Mater.*, 2022, **32,** 2112711.

[2] S. Guan, W. Wang, J. Zheng and C. Xu, *Electrochim. Acta*, 2020, **354,** 136702.

[3] X. Yang, S. Cong, J. Li, J. Chen, F. Jin and Z. Zhao, *Sol. Energy Mater. Sol. Cells*, 2019, 200, 109952.

[4] W. Wang, S. Guan, M. Li, J. Zheng and C. Xu, *Org. Electron.*, 2018, **56,** 268-275.

[5] G. Xing, G. Kuang, Y. Tao, Y. Wang, Y. Kang, Y. Guo and S. Zhang, *Sol. Energy Mater. Sol. Cells*, 2022, **248,** 111968.

[6] V. Primiceri, M. Pugliese, C. T. Prontera, A. G. Monteduro, M. Esposito, A. Maggiore, A. Cannavale, R. Giannuzzi, G. Gigli, V. Maiorano, Low-cost gel polymeric electrolytes for electrochromic applications. *Sol. Energy Mater. Sol. Cells*, 2022, **240,** 111657.

[7] P. Chen, X. Liang, J. Wang, D. Zhang, S. Yang, W. Wu, W. Zhang, X. Fan and D. Zhang, *J Sol-gel Sci. Technol.*, 2017, **81,** 850-858.

[8] H. Gong, A. Li, G. Fu, M. Zhang, Z. Zheng, Q. Zhang, K. Zhou, J. Liu and H. Wang, *J. Mater. Chem. A*, **2023,** 11, 8939–8949.

[9] Y. Ding, M. Wang, Z, Mei, X. Diao, *ACS Appl. Mater. Interfaces*, 2023, **15,** 15646-15656.

[10] L. Liu, X. Diao, Z. He, Y. Yi, T. Wang, M. Wang, J. Huang, X. He, X. Zhong and K. Du, *Energy Storage Mater.*, 2020, **33,** 258-267.

[11] J. Bae, M. K. Song, Y. J. Park, J. M. Kim, M. Liu and Z. L. Wang, Angew. Chem. Inter. Ed., 2011, 50, 1683-1687.

[12] Y. Meng, Y. Zhao, C. Hu, H. Cheng, Y. Hu, Z. Zhang, G. Shi and L. Qu, Adv. Mater., 2013, 25, 2326-2331.

[13] Y. Chen, X. Li, Z. Bi, G. Li, X. He and X. Gao, Chem. Eng. J., 2018, 353, 499-506.

[14] Z. Tong, T. Kang, Y. Wan, R. Yang, Y. Wu, D. Shen, S. Liu, Y. Tang and C.-S. Lee, Adv. Funct. Mater., 2021, 31, 2104639.

[15] Z. Tong, R. Lian, R. Yang, T. Kang, J. Feng, D. Shen, Y. Wu, X. Cui, H. Wang, H. Wang, Y. Tang and C.-S. Lee, Energy Storage Mater., 2022, 44, 497-507.